

## Probing the size-structure-property correlation of individual nanowires

Binni Varghese,<sup>1,2</sup> Yousheng Zhang,<sup>2,3</sup> Yuan Ping Feng,<sup>1</sup> Chwee Teck Lim,<sup>2,3,4,\*</sup> and Chorong-Haur Sow<sup>1,2,†</sup>

<sup>1</sup>*Department of Physics, Faculty of Science, National University of Singapore, 2 Science Drive 3, Singapore 117542*

<sup>2</sup>*National University of Singapore Nanoscience and Nanotechnology Initiative (NUSNNI), 2 Science Drive 3, Singapore 117542*

<sup>3</sup>*Division of Bioengineering, National University of Singapore, 9 Engineering Drive 1, Singapore 117576*

<sup>4</sup>*Department of Mechanical Engineering, National University of Singapore, 9 Engineering Drive 1 Singapore 117576*

(Received 17 October 2008; revised manuscript received 26 December 2008; published 16 March 2009)

We report a combinatory approach to correlate physical properties with microstructure of individual nanowires (NWs). The mechanical and electrical-transport properties of individual Nb<sub>2</sub>O<sub>5</sub> NWs are determined experimentally and correlated with the microscopic structures of the same NW. The observed diameter-dependent variation in the Young's modulus is attributed to the defect density variation among NWs of different size. The two-probe electrical-transport measurements revealed the semiconducting nature of Nb<sub>2</sub>O<sub>5</sub> NWs. A gradual increase in the electrical conductivity of the NW with diameter was observed.

DOI: [10.1103/PhysRevB.79.115419](https://doi.org/10.1103/PhysRevB.79.115419)

PACS number(s): 61.46.Km

### I. INTRODUCTION

Advances in nanofabrication techniques offered additional handles to tune material properties by altering the physical size and shape of the nanomaterials.<sup>1–3</sup> Physical properties of nanosized materials are primarily determined by (i) spatial confinement effects, (ii) nature of the surfaces, and (iii) its microstructural details. All these factors are sensitively dependent on the characteristic size of the nanostructures. Most of the “bottom up” nanofabrication approaches yield structures with a size distribution, and hence the information obtained from the characterization of an array of as-synthesized products gives rise to averaged results and does not reflect the unique properties of individual nanostructures. In addition, physical properties of every nanostructure are largely determined by its microstructure (e.g., crystal quality, type, and concentration density of defects). Hence, an approach that facilitates both the characterization of physical properties and revelation of microscopic structural details of individual nanostructures is essential. In this work, a combinatory approach to elucidate size-structure-property correlation of individual nanowire (NW) is demonstrated.

We have chosen niobium pentoxide (Nb<sub>2</sub>O<sub>5</sub>) NWs to investigate the size-structure-property relationship at the nanoscale. Nb<sub>2</sub>O<sub>5</sub> is an intrinsically *n*-type semiconductor with a wide band gap of  $\sim 3.4$  eV.<sup>4</sup> Nb<sub>2</sub>O<sub>5</sub> is a well-known electrochromic and sensing material.<sup>5,6</sup> Its metal excess nonstoichiometric phase is known for strange magnetic and electrical properties at a reasonably high temperature.<sup>7</sup> Recently a few reports focused on the controlled synthesis of Nb<sub>2</sub>O<sub>5</sub> NWs.<sup>8,9</sup> In addition, vertically oriented Nb<sub>2</sub>O<sub>5</sub> NW arrays were found to exhibit excellent electron field-emission capability.<sup>8</sup> Due to the intrinsic semiconducting nature of Nb<sub>2</sub>O<sub>5</sub>, its nanostructures could have potential applications in nanoelectronics or nanoelectromechanical systems. As a prerequisite to the realization of such applications, the characterization of the physical properties of individual Nb<sub>2</sub>O<sub>5</sub> nanostructures and proper understanding on the evolution of their properties with size are critical.

Figure 1 depicts the experimental approach adopted to probe the effect of size and microstructures on the physical

properties of individual NWs. The measurements were performed on suspended NWs, which are assembled by drying a droplet of aqueous suspension of NWs across the holes on a SiN TEM grid. Such NW bridges were secured by depositing Pt at both ends using focused ion beam (FIB) [Fig. 1(a)]. The mechanical characterization of these isolated NW bridges was performed by nanoscale three-point bend test using atomic force microscopy (AFM) [Fig. 1(b)]. Two-probe electric transport measurements were carried out in a field-emission scanning electron microscope (FESEM) equipped with nanomanipulators [Fig. 1(c)]. A detailed microstructural investigation on the same NW was performed by high-resolution transmission electron microscopy (HRTEM) [Fig. 1(d)]. Using the combinatory approach presented in this work, we are able to measure the physical properties of selected NWs with a view into their microscopic structures. This technique provides valuable insight into the correlation between microstructure of NWs directly with its physical properties.

### II. RESULTS AND DISCUSSIONS

Crystalline Nb<sub>2</sub>O<sub>5</sub> NWs were synthesized by adopting our previously reported method.<sup>8</sup> In brief, vertically oriented Nb<sub>2</sub>O<sub>5</sub> NWs were synthesized directly on Nb foils by heating at 900 °C in a horizontal tube furnace under a controlled flow of Ar and oxygen gases. The as-synthesized NWs can be suspended in distilled water by ultrasonic agitation. A few drops of this NW solution were dried on a SiN TEM grid (DuraSIN™) with circular holes of diameter  $\sim 2$   $\mu$ m. After drying, isolated NWs bridging across the holes were selected for the mechanical and electrical characterization tests. In a dual-beam high-resolution focused ion-beam system (Quanta 200–3D FIB-SEM, FEI Co.), the NW bridges were first imaged using electron beam and the location was noted for subsequent experiments. Pt was deposited at the both ends of each selected NW bridge using ion beam. The SEM image displayed as Fig. 2(a) exemplifies one of the NW bridge and Fig. 2(b) shows the SEM image captured after Pt deposition at the ends of the bridge. The thickness of the Pt deposited was  $\sim 100$  nm. Pt deposited at the ends of the NW bridges

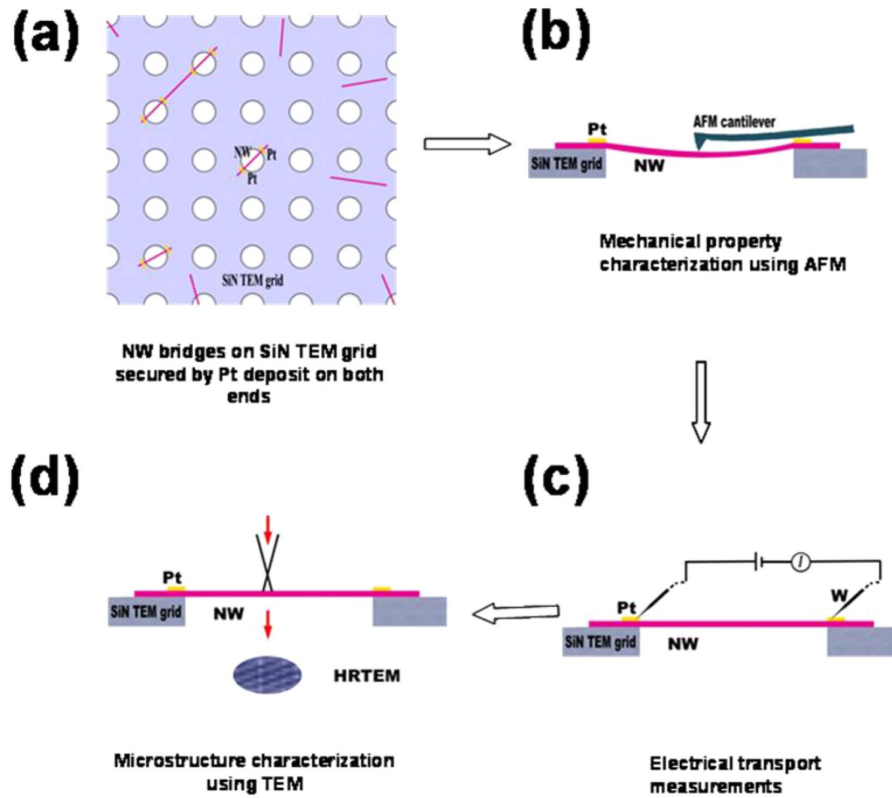


FIG. 1. (Color online) Schematic illustration of experimental procedure adopted to obtain structure-physical-property correlation in individual NWs. (a) Construction of end clamped isolated NW bridges on SiN TEM grid with circular holes. (b) Mechanical property characterization of individual NWs by nanoscale three-point bend test. (c) Electrical transport property characterization of individual NWs by two-probe measurements. (d) Characterization of microstructure of the NWs by HRTEM.

served two purposes. First, the NWs were secured in place avoiding slipping during the three-point bend test to characterize their mechanical properties. Second, the “Pt-tapes” functioned as the contact pad for the electrical characterization of the NW. Being constructed on the TEM grid, each NW bridge can be examined by TEM to reveal the details of the microstructures.

**A. Mechanical properties of Nb<sub>2</sub>O<sub>5</sub> nanowires**

The mechanical characterization the NWs was performed by nanoscale three-point bend test using atomic force microscopy (AFM, Dimension 3100, Nanoscope Digital Instruments). The area with the NW bridge was imaged by the force-volume (*F-V*) mode. From the as obtained *F-V* image the force curve right at the midpoint of the NW bridge was

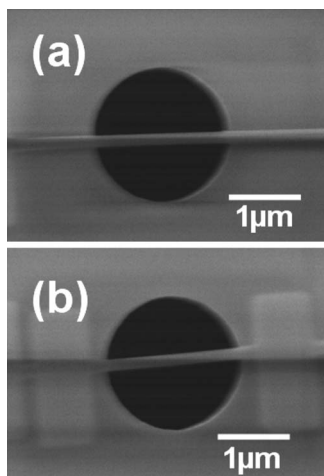


FIG. 2. SEM image of the Nb<sub>2</sub>O<sub>5</sub> NW bridge across the hole on a SiN TEM grid, (a) before and (b) after deposition of Pt at the ends of the NW bridge.

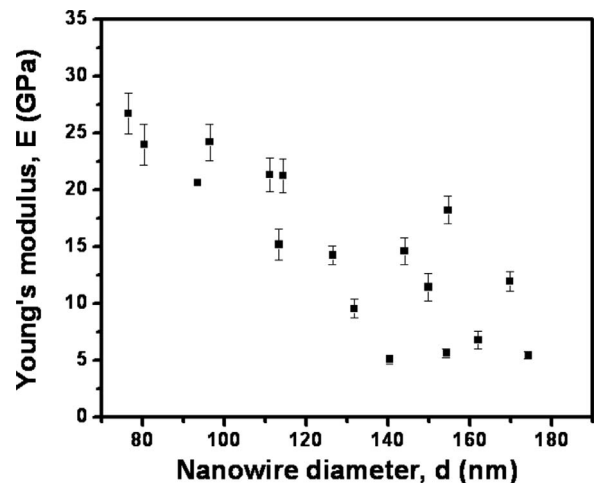


FIG. 3. Plot of Young’s modulus of Nb<sub>2</sub>O<sub>5</sub> NWs as a function of the NW diameter.

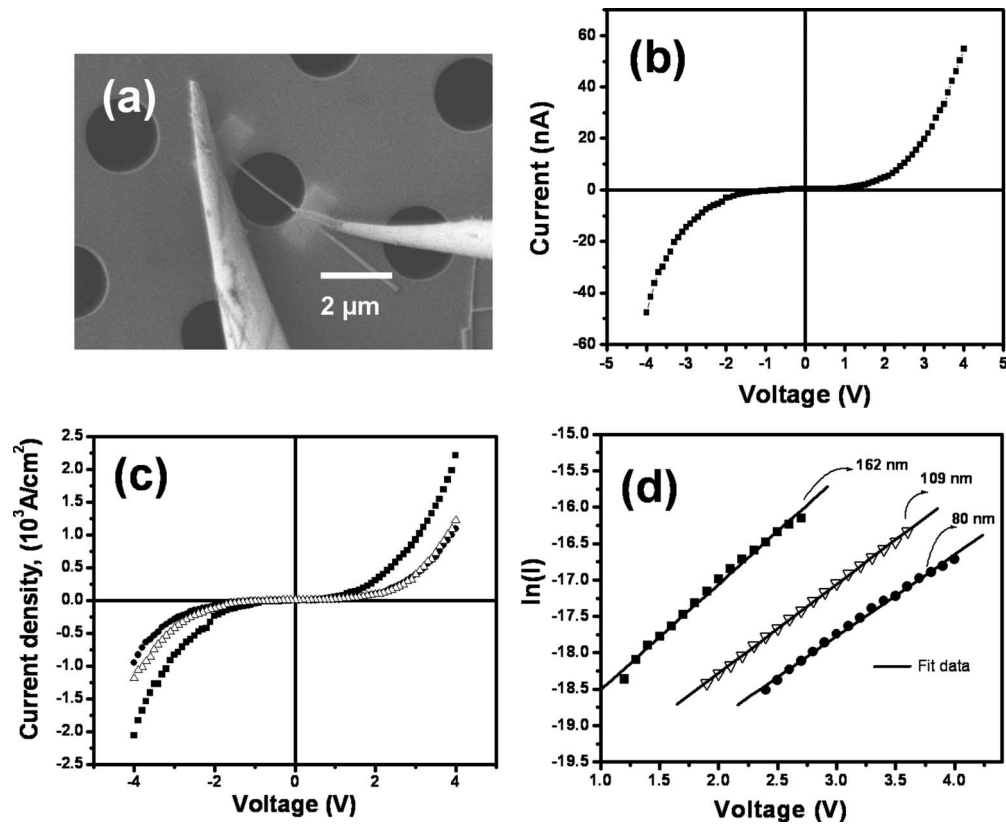


FIG. 4. Electrical transport properties of  $\text{Nb}_2\text{O}_5$  NWs. (a) SEM image of a NW bridge of diameter  $\sim 80$  nm showing the electrical probing. (b)  $I$ - $V$  characteristics of the same NW. (c) Current density versus voltage for three NWs of diameter 80 nm (solid circles), 109 nm (open triangles) and 162 nm (solid squares). The length of the NW in between the Pt pads was  $\sim 2$   $\mu\text{m}$ . (d) plot of  $\ln(I)$  versus voltage of three NWs with different diameter. The solid curves are the corresponding linear fit.

selected for calculating the Young's modulus as described in earlier reports.<sup>9,10</sup> For the three-point bend test, silicon nitride AFM cantilever of nominal force constant 0.57 N/m with tip size of 15–20 nm (OTR8, Veeco Inc.) was used. Before the test, the AFM cantilever was calibrated using the technique described elsewhere.<sup>11</sup> Considering the NW bridge as a beam with both ends fixed and of uniform circular cross section, Young's modulus,  $E$  is calculated according to

$$E = \frac{Fl^3}{3\pi d^4 \delta}, \quad (1)$$

where  $F$  is applied force,  $l$  is suspended length of the NW bridge,  $d$  is diameter of NW, and  $\delta$  is deflection at the mid-point of the NW. To minimize error in calculations, the suspended length and the diameter of NWs was estimated from the SEM images. NWs with sizes in the range of 80 to 180 nm were investigated. A plot of the measured Young's modulus of the NW versus diameter is displayed in Fig. 3. The Young's modulus fall in the range of 5–30 GPa. Thus, the Young's modulus of the  $\text{Nb}_2\text{O}_5$  NW shows a size-dependent variation. The elastic modulus significantly increases as the diameter reduces. The Young's modulus of NWs is significantly higher than that of the reported  $\text{Nb}_2\text{O}_5$  film (0.8 GPa).<sup>12</sup> The better crystalline quality of NWs compared to the polycrystalline film is likely to be the primary reason for the difference in Young's modulus.

## B. Electrical transport properties of $\text{Nb}_2\text{O}_5$ nanowires

With the NWs padded with Pt and fabricated on insulating SiN surface, electrical-transport measurements on the NW bridges can be directly performed. Two probe electric transport measurements were carried out in a FESEM (JSM7401-F, JEOL) equipped with nanomanipulators (Prober Nano-M, Zyvex Instruments). A Keithley source-measure unit (model: 4200SCS) connected to the tungsten probes was used to measure the current-voltage ( $I$ - $V$ ) characteristics of the NWs. All the transport measurements were carried out at room temperature at a base pressure of  $\sim 1 \times 10^{-4}$  Pa. Two probe electronic transport measurements were carried out using tungsten probes of tip size  $\sim 50$  nm. A typical SEM image of the NW bridge of diameter  $\sim 80$  nm captured during electrical probing is displayed in Fig. 4(a). The distance between the Pt pad electrodes was  $\sim 2$   $\mu\text{m}$ . The  $I$ - $V$  characteristic obtained from this NW is shown in Fig. 4(b). The nonlinear  $I$ - $V$  curve demonstrated the typical semiconducting characteristics of the  $\text{Nb}_2\text{O}_5$  NW. We note that the curve is reasonably symmetrical in the positive and negative bias conditions. Using the geometrical parameters estimated from the SEM image and  $I$ - $V$  characteristics at a bias range of 2–4 V, the conductivity ( $\sigma$ ) of the NW was found to vary between  $1 \times 10^{-2}$ – $1 \times 10^{-4}$  ( $\Omega \cdot \text{cm}$ )<sup>-1</sup>. A plot of current density versus voltage of three NWs with diameters  $\sim 80$  nm (solid circles), 109 nm

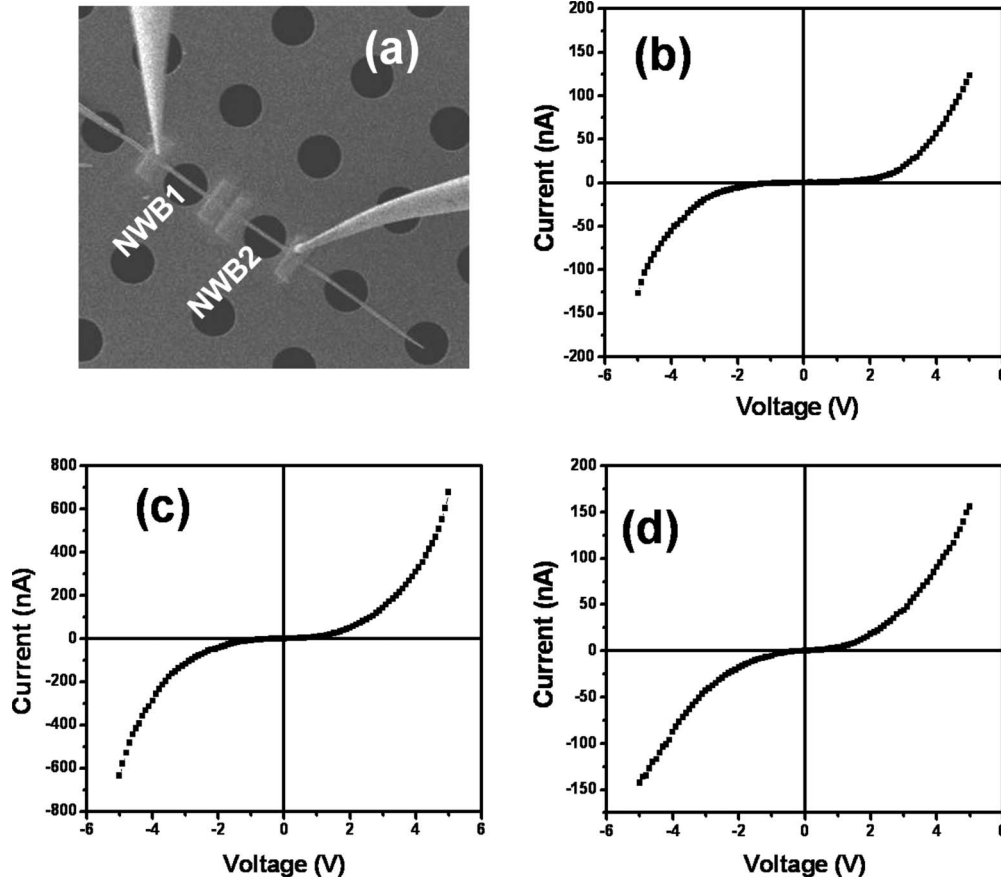


FIG. 5. Electrical transport through tapered  $\text{Nb}_2\text{O}_5$  NWs. (a) SEM showing the electrical probing on a tapered NW forming two “NW bridges” (labeled NWB1 and NWB2) across holes in SiN TEM grid. (b)  $I$ - $V$  curve when the circuit includes both NW bridges.  $I$ - $V$  characteristics of the (c) NWB1 and (d) NWB2.

(open triangles), and 162 nm (solid squares) is shown in Fig. 4(c). An obvious increase in the current density ( $J$ ) for a particular voltage with increase in diameter of the NW was observed. The conductivity is given by the equation  $\sigma = (\frac{dI}{dV})l$ , where  $l$  is the length of the NW in between the contact pads. The length of the NW in between the contact pads is the same ( $\sim 2 \mu\text{m}$ ) for all the tested NWs, and this implies a gradual increase in the conductivity with diameter of the NWs. We note that the previously reported electrical conductivity of bulk  $\text{Nb}_2\text{O}_5$  [ $1 \times 10^{-3}$  to  $1 \times 10^{-6}$  ( $\text{ohm}\cdot\text{cm}$ ) $^{-1}$ ] is close to the estimated NW conductivity.<sup>13</sup>

The NW with metal pads on either side can be modeled as a metal-semiconductor-metal circuit. Due to the work-function difference between the  $\text{Nb}_2\text{O}_5$  NW [work function,  $\varphi \sim 5.6$  eV (Ref. 14)] and Pt metal (work function,  $\varphi \sim 6.1$  eV) pads the two contacts form Schottky type barriers. This circuit is equivalent to two Schottky diodes connected back to back through a semiconductor.<sup>15</sup> The  $I$ - $V$  characteristic of such circuit at intermediate bias condition is determined by the reverse biased Schottky junction. Assuming the thermionic field-emission theory for the reverse biased Schottky junction the current-voltage relationship for such circuit at intermediate bias conditions can be expressed as<sup>15,16</sup>

$$\ln I = \ln(S) + V \left( \frac{e}{kT} - \frac{1}{E_0} \right) + \ln J_s, \quad (2)$$

where  $S$  is an area factor,  $e$  is electronic charge,  $k$  is Boltzmann’s constant ( $1.38 \times 10^{-23} \text{ m}^2 \text{ kg s}^{-2} \text{ K}^{-1}$ ),  $T$  is temperature, and  $J_s$  is a slowly varying function of the applied voltage.  $E_0$  is a function of carrier density ( $n$ ) and is given by the equation,  $E_0 = E_{00} \coth(\frac{eE_{00}}{kT})$ , where  $E_{00} = (\frac{\hbar}{2}) (\frac{n}{m^* \epsilon_s \epsilon_0})^{1/2}$ , with  $m^*$  is the effective mass of electron in  $\text{Nb}_2\text{O}_5$  NW,  $\epsilon_s$  is its relative permittivity [ $\epsilon_s\{\text{Nb}_2\text{O}_5\} \sim 41$ ], and  $\epsilon_0$  is the permittivity of free space. This implies that the slope of  $\ln(I)$  versus voltage curve can be approximated to  $\frac{e}{kT} - \frac{1}{E_0}$ . The electron effective mass of the  $\text{Nb}_2\text{O}_5$  was calculated using first-principles method based on the density-functional theory and the Vienna *ab initio* Simulation package (VASP).<sup>17–19</sup> Energy band of bulk  $\text{Nb}_2\text{O}_5$  along the [110] direction near the conduction-band minimum at  $\Gamma$  was calculated and fitted to a parabola to derive the electron effective mass. Figure 4(d) shows the plot of  $\ln(I)$  versus  $V$  for three different NWs of diameters 162, 109, and 80 nm. From the slope of the linear fitted curve, and using the calculated effective mass of  $0.76m_0$  for  $\text{Nb}_2\text{O}_5$ , the electron density of each specific NWs was calculated. The estimated electron densities for the NWs of diameters 162, 109, and 80 nm are  $2.25 \times 10^{21}/\text{cm}^3$ ,

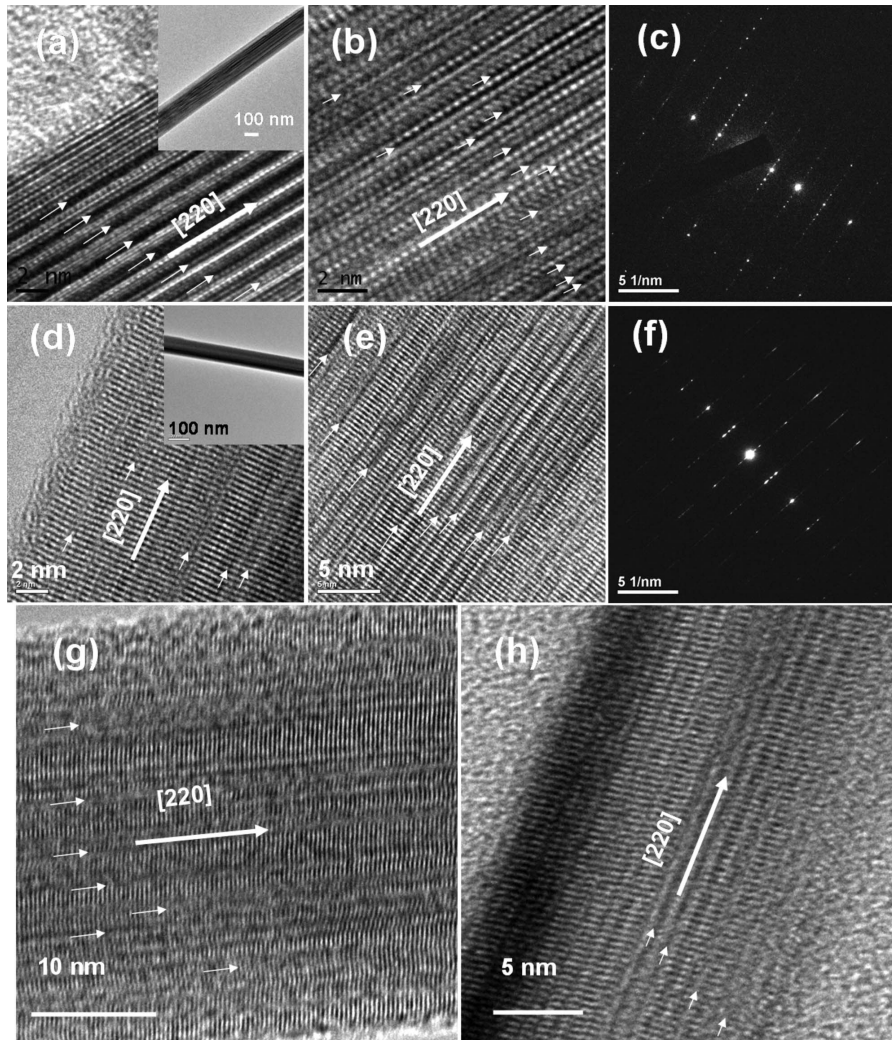


FIG. 6. Microstructures of  $\text{Nb}_2\text{O}_5$  NWs. [(a) and (b)] HRTEM image captured near the edge and core region of a NW of diameter  $\sim 180$  nm. Inset of (a) is a low magnification TEM image of the same NW and (c) its SAED pattern. [(d) and (e)] HRTEM image captured near the edge and core region of a NW of diameter  $\sim 80$  nm. A low-magnification TEM image of the same NW is displayed in the inset of (d) and (f) its SAED pattern. [(g) and (h)] HRTEM images of  $\text{Nb}_2\text{O}_5$  NWs of diameter  $\sim 35$  and  $\sim 15$  nm, respectively. Arrows in the HRTEM images highlight the planar defects.

$1.87 \times 10^{21}/\text{cm}^3$ , and  $1.71 \times 10^{21}/\text{cm}^3$ , respectively. The calculated carrier density ratio among these three NWs was 1:0.83:0.76, with a clear indication of increase in carrier density with size. This implies that the observed high conductivity of larger NWs is likely due to the relatively high carrier density.

Our synthesis method produced many of the NWs with nonuniform cross section along the length.<sup>8</sup> Typically one can find NWs with a broader base and sharper tip. We have investigated the electrical-transport properties of such tapered NWs. Figure 5(a) shows SEM image of a single tapered NW forming two “NW bridges” (labeled NWB1 and NWB2) across the holes in the SiN TEM grid. The average diameter of NWB1 and NWB2 is 156 and 124 nm, respectively.  $I$ - $V$  measurements on this NW were carried out in three different configurations. In the first configuration, the circuit includes both bridges (NWB1+NWB2) and the corresponding  $I$ - $V$  curve is shown in Fig. 5(b). In the second configuration the  $I$ - $V$  curve was recorded through the NW

bridge with larger diameter (NWB1) and is displayed in Fig. 5(c). In this configuration, an obvious increase in conductivity compared to the first configuration was observed. Finally, the  $I$ - $V$  curve across the NW bridge with smaller diameter (NWB2) was recorded and displayed in Fig. 5(d). The  $I$ - $V$  curve across the smaller NW bridge was similar to the  $I$ - $V$  curve obtained from the first configuration. These results suggest that the electron transport through the tapered NW is dominated by the thinner and more resistive part.

### C. Characterization of microstructures of the $\text{Nb}_2\text{O}_5$ nanowires

After performing three-point bend test and two-probe electrical measurements, the microstructures of NWs were investigated on a one by one basis. Extensive HRTEM (JEM-2010F, 200 kV, JEOL) studies revealed that the growth direction of all the NWs are uniquely along the [220] direction. Figure 6(a) shows a typical HRTEM image near the edge of a NW of diameter  $\sim 180$  nm. A low magnification TEM im-

age of the NW is shown in the inset of Fig. 6(a). The NW surface is clean and free from any amorphous coating. Large density of planar defects (stacking faults, dislocations, etc.) along the long axis of the NW was observed in the HRTEM (the planar defects are highlighted by the arrows). Defects were observed in the core region of the NW as well [Fig. 6(b)]. Presence of planar defects in this NW was further evident from the streaking of its selected area electron diffraction (SAED) pattern along the [220] direction [Fig. 6(c)]. Figures 6(d) and 6(e) show HRTEM images near the edge and core region of a NW of diameter  $\sim 80$  nm. A low-magnification TEM image of the same NW is displayed in the inset of Fig. 6(d) and its SAED pattern is displayed in Fig. 6(f). Compared to the bigger NWs, a relatively low planar defect density was observed in the HRTEM of this NW. In this study, more than ten NWs having various diameters were examined using HRTEM. Although planar defects were observed even in the smallest investigated NW of diameter  $\sim 15$  nm, relative densities of the planar defects were found to significantly decrease with size (HRTEM images of NWs with diameters  $\sim 35$  and  $\sim 15$  nm are shown in Figs. 6(g) and 6(h), respectively).

The relationship between mechanical properties and structure of micro-sized and nano-sized materials has been addressed by many researchers.<sup>20–28</sup> In micron-sized crystals, the observed size-dependent elastic properties have been attributed to the dislocation motion and related phenomenon under deformation.<sup>20</sup> On the other hand, it is generally accepted that the surface elasticity is critical in determining the elastic properties at the nanoscale.<sup>21–29</sup> The size-dependent variation in elastic constants at the nanoscale can be explained on the basis of variations in the degree of surface contribution with respect to size. In addition, the presence of internal structural defects was found to have large effects on the elastic constants of nanoscale materials.<sup>30,31</sup> Relatively large size of NWs investigated in this study ( $>80$  nm) suggests that the surface contribution have less effect on the measured elastic constant. The defect density variation among NWs of different size is likely to be the determining factor of the size-dependent elastic modulus. The interatomic separation near a planar defect would be different from the perfect crystal. A crystal with defects can be considered as a heterogeneous system of perfect and defective regions. The apparent modulus of such system is related to the average stresses and strain distribution in the material under external force.<sup>32</sup> Previous theoretical studies suggested that an elongation in the interatomic distance at the vicinity of a defect compared to the perfect crystal decreases the apparent Young's modulus.<sup>33</sup> Since NWs with larger diameter comprises high density of defects compared to relatively smaller ones, the elastic modulus decreases with increase in size. The observed scattering in the data for the estimated Young's

modulus of the NWs with similar diameter can be explained on the basis of defect density variations.

The diameters of the NWs studied in this work are considerably larger than the strong confinement regime ( $<10$  nm), band-gap modification with size is unlikely to play any significant role on the observed conductivity increase with size. It is reported that the conduction in  $\text{Nb}_2\text{O}_5$  is primarily due to the oxygen deficiency related defects.<sup>13,34</sup> Each oxygen vacant site traps one or two electrons from the metal. The energy levels of such trapped electrons are close to the conduction band of the Nb metal. These electrons contribute to the conductivity of the  $\text{Nb}_2\text{O}_5$  significantly. Thus the electrical conductivity in  $\text{Nb}_2\text{O}_5$  largely depends on the oxygen vacancy defects. It is worth mentioning that the reported experimentally estimated oxygen vacancies in bulk  $\text{Nb}_2\text{O}_5$  is in the order of  $1 \times 10^{21}/\text{cm}^3$  and is the same as our electron density calculated from the two-probe  $I$ - $V$  measurements.<sup>35</sup> Since oxygen vacancies are the prominent defect structures in  $\text{Nb}_2\text{O}_5$ , it is very likely that the observed planar defects could be originated from rows of missing oxygen atoms. Due to the presence of large density of such planar defects in larger NWs the carrier density increases and exhibits high electrical conductivity than the thinner ones.

### III. SUMMARY

In conclusion, we have developed an approach which enables both the characterization of physical properties and identification of microscopic structural details of the same NW. The mechanical and electrical-transport properties  $\text{Nb}_2\text{O}_5$  NWs were investigated. Our studies revealed a “size effect” on the Young's modulus of the  $\text{Nb}_2\text{O}_5$  NWs with an apparent increase in the elastic modulus with decrease in size. The relatively large density planar defects observed in NWs of larger diameter are likely to be the primary reason for the size-dependent elastic properties. The two-probe electronic transport measurements demonstrated the characteristic semiconducting nature of the  $\text{Nb}_2\text{O}_5$  NWs. The observed size-dependent conductivity can be explained on the basis of oxygen vacancy related defect density variation with size. Our studies demonstrated the potential of  $\text{Nb}_2\text{O}_5$  NWs as nanoelectronic components or nanoelectromechanical applications. Finally, we believe that the combinatory approach described here can be extended to obtain size-structure-property correlation of other nanostructures as well.

### ACKNOWLEDGMENTS

This work is funded by the Science and Engineering Research Council (SERC) of the Agency for Science, Technology and Research (A\*STAR). Their support is gratefully acknowledged.

\*Corresponding author. mpelimct@nus.edu.sg

†Corresponding author. FAX: (65) 67776126.  
physowch@nus.edu.sg

- <sup>1</sup>H. Yu, J. Li, R. A. Loomis, L. W. Wang, and W. E. Buhro, *Nature Mater.* **2**, 517 (2003).
- <sup>2</sup>S. Kan, T. Mokari, E. Rothenberg, and U. Banin, *Nature Mater.* **2**, 155 (2003).
- <sup>3</sup>B. Varghese, C. H. Teo, Z. Yanwu, M. V. Reddy, B. V. R. Chowdari, A. T. S. Wee, T. B. C. Vincent, C. T. Lim, and C. H. Sow, *Adv. Funct. Mater.* **17**, 1932 (2007).
- <sup>4</sup>N. Özer, D. G. Chen, and C. M. Lampert, *Thin Solid Films* **277**, 162 (1996).
- <sup>5</sup>D. Rosenfeld, P. E. Schmid, S. Szeles, F. Levy, V. Demarne, and A. Grisel, *Sens. Actuators B* **37**, 83 (1996).
- <sup>6</sup>M. Mozetič, U. Cvelbar, M. K. Sunkara, and S. Vaddiraju, *Adv. Mater. (Weinheim, Ger.)* **17**, 2138 (2005).
- <sup>7</sup>R. J. Cava, B. Batlogg, J. J. Krajewski, P. Gammel, H. F. Poulsen, W. F. Peck, Jr., and L. W. Rupp, Jr., *Nature (London)* **350**, 598 (1991).
- <sup>8</sup>B. Varghese, C. H. Sow, and C. T. Lim, *J. Phys. Chem. C* **112**, 10008 (2008).
- <sup>9</sup>F. C. Cheong, B. Varghese, Y. Zhu, E. P. S. Tan, L. Dai, V. B. C. Tan, C. T. Lim, and C. H. Sow, *J. Phys. Chem. C* **111**, 17193 (2007).
- <sup>10</sup>E. P. S. Tan and C. T. Lim, *Appl. Phys. Lett.* **84**, 1603 (2004).
- <sup>11</sup>A. Torii, M. Sasaki, K. Hane, and S. Okuma, *Meas. Sci. Technol.* **7**, 179 (1996).
- <sup>12</sup>K. E. Petersen, *IEEE Trans. Electron Devices* **25**, 1241 (1978).
- <sup>13</sup>E. H. Greener, D. H. Whitmore, and M. E. Fine, *J. Chem. Phys.* **34**, 1017 (1961).
- <sup>14</sup>I. Lindau and W. E. Spicer, *J. Appl. Phys.* **45**, 3720 (1974).
- <sup>15</sup>Z. Y. Zhang, C. H. Jin, X. L. Liang, Q. Chen, and L. M. Peng, *Appl. Phys. Lett.* **88**, 073102 (2006).
- <sup>16</sup>Z. Zhang, K. Yao, Y. Liu, C. Jin, X. Liang, Q. Chen, and L. M. Peng, *Adv. Funct. Mater.* **17**, 2478 (2007).
- <sup>17</sup>G. Kresse and J. Hafner, *Phys. Rev. B* **47**, 558 (1993).
- <sup>18</sup>G. Kresse and J. Hafner, *Phys. Rev. B* **48**, 13115 (1993).
- <sup>19</sup>G. Kresse and J. Furthmüller, *Comput. Mater. Sci.* **6**, 15 (1996).
- <sup>20</sup>M. D. Uchic, D. M. Dimiduk, J. N. Florando, and W. D. Nix, *Science* **305**, 986 (2004).
- <sup>21</sup>C. Q. Chen, Y. Shi, Y. S. Zhang, J. Zhu, and Y. J. Yan, *Phys. Rev. Lett.* **96**, 075505 (2006).
- <sup>22</sup>G. Y. Jing, H. L. Duan, X. M. Sun, Z. S. Zhang, J. Xu, Y. D. Li, J. X. Wang, and D. P. Yu, *Phys. Rev. B* **73**, 235409 (2006).
- <sup>23</sup>S. Cuenot, C. Fréty, S. C. Demoustier, and B. Nysten, *Phys. Rev. B* **69**, 165410 (2004).
- <sup>24</sup>H. Liang, M. Upmanyu, H. Huang, *Phys. Rev. B* **71**, 241403(R) (2005).
- <sup>25</sup>W. E. Wong, P. E. Sheehan, and C. M. Lieber, *Science* **277**, 1971 (1997).
- <sup>26</sup>A. Kis, D. Mihailovic, M. Remskar, A. Mrzel, A. Jesih, I. Piwonski, A. J. Kulik, W. Benoit, and L. Forro, *Adv. Mater. (Weinheim, Ger.)* **15**, 733 (2003).
- <sup>27</sup>X. Tao and X. Li, *Nano Lett.* **8**, 505 (2008).
- <sup>28</sup>M. F. Yu, O. Lourie, M. J. Dyer, K. Moloni, T. F. Kelly, and R. S. Ruoff, *Science* **287**, 637 (2000).
- <sup>29</sup>G. Stan, C. V. Ciobanu, P. M. Parthangal, and R. F. Cook, *Nano Lett.* **7**, 3691 (2007).
- <sup>30</sup>C. M. Salerno and J. P. Watt, *J. Appl. Phys.* **60**, 1618 (1986).
- <sup>31</sup>B. Varghese, Y. S. Zhang, L. Dai, V. B. C. Tan, C. T. Lim, and C. H. Sow, *Nano Lett.* **8**, 3226 (2008).
- <sup>32</sup>I. Alber, J. L. Bassani, M. Khantha, V. Vitek, and G. J. Wang, *Philos. Trans. R. Soc. London, Ser. A* **339**, 555 (1992).
- <sup>33</sup>D. Wolf and J. F. Lutsko, *Phys. Rev. Lett.* **60**, 1170 (1988).
- <sup>34</sup>E. H. Greener, G. A. Fehr, and W. M. Hirthe, *J. Chem. Phys.* **38**, 133 (1963).
- <sup>35</sup>R. F. Janninck and D. H. Whitmore, *J. Chem. Phys.* **37**, 2750 (1962).